Int. J. Electrochem. Sci., 13 **(2018)** xx – yy

International Journal of ELECTROCHEMICAL SCIENCE
www.electrochemsci.org

TiO_2/MoO_2 Nanocomposite as Anode Materials for High Power Li-ion Batteries with Exceptional Capacity

Dustin Bauer[1,2], Alexander J. Roberts[3], Chris L. Starkey[1], Raman Vedarajan[2], Dan J.L. Brett[4], Paul R. Shearing[4], Noriyoshi Matsumi[2] and Jawwad A. Darr[1,]*

[1] Department of Chemistry, University College London, 20 Gordon Street, London, WC1H 0AJ, U.K.
[2] School of Materials Science, Japan Advanced Institute of Science and Technology, 1-1 Asahidai, Nomi, Ishikawa, Japan
[3] WMG, University of Warwick, CV4 7AL Coventry, UK
[4] Electrochemical Innovation Lab, Department of Chemical Engineering, University College London, Torrington Place, London, WC1E 7JE, U.K.
[*]E-mail: j.a.darr@ucl.ac.uk

Received: 1 xxx 2018 / *Accepted:* 1 xxx 2018 / *Published:* 1 xxx 2018

Nanoparticles of molybdenum(IV) oxide (MoO_2) and a TiO_2/MoO_2 nanocomposite were synthesised via a continuous hydrothermal synthesis process. Both powders were analysed using XRD, XPS, TEM, and BET and evaluated as active materials in anodes for Li-ion half-cells. Cyclic voltammetry and galvanostatic charge/discharge measurements were carried out in the potential window of 0.1 to 3.0 V vs. Li/Li^+. Specific capacities of ca. 350 mAh g^{-1} were obtained for both materials at low specific currents (0.1 A g^{-1}); TiO_2/MoO_2 composite electrodes showed superior rate behaviour & stability under cycling (compared to MoO_2), with stable specific capacities of ca. 265 mAh g^{-1} at a specific current of 0.5 A g^{-1} and ca. 150 mAh g^{-1} after 350 cycles at a specific current of 2.5 A g^{-1}. The improved performance of the composite material compared to MoO_2 was attributed to a smaller particle size, improved stability to volume changes (during cycling), and lower charge transfer resistance during cycling. Li-ion hybrid electrochemical capacitors using TiO_2/MoO_2 composite anodes and activated carbon (AC) cathodes were evaluated and showed excellent performance with an energy density of 44 Wh kg^{-1} at a power density of 600 W kg^{-1}.

Keywords: continuous hydrothermal flow synthesis; molybdenum oxide; composite anode materials; pseudocapacitance; supercabattery

1. INTRODUCTION

Energy storage devices have become a major research focus because of concerns over global warming, energy security, intermittency of renewable energy supplies and air pollution [1]. As hybrid and full electric vehicles become more readily available and sought after, they enable a decarbonisation of the transport sector [2]. The key technology making this transition possible is Li-ion batteries (LIBs), which can be used in both automotive and stationary energy storage applications [3–6]. Typically, a LIB consists of an anode (e.g. graphite), a cathode (e.g. lithium iron phosphate), an electronically insulating separator (glass fibre or polyethylene) and an organic electrolyte containing a Li^+ salt [7]. Because power densities of LIBs are often limited, electrochemical double-layer capacitors (EDLC) are considered more promising for high-power applications such as regenerative breaking [8]. More recently, devices such as Li-ion hybrid electrochemical capacitors (Li-HEC) have been developed as they offer a balance of both moderate power and energy density; these devices typically use activated carbon cathodes and battery-type redox anodes. During the charging of Li-HECs, Li^+ is inserted into the anode active material and anions (e.g. hexafluorophosphate) are absorbed onto the active carbon in the cathode (PF_6^- desorption and Li^+ extraction occur during discharge) [9]. In contrast to LIBs, both anions and cations are subject to symmetrical driving forces to opposite electrodes [10], which means that concentration gradients, which limit high power performance in LIBs, are reduced [11].

Nanomaterials are of interest as active electrode materials in high-power LIBs because of their high surface area to volume ratio, which can result in a higher proportion of charge storage on or near the surface, enabling more rapid charge transfer compared to majority intercalation micron-sized materials with relatively lower surface areas [12,13]. This is particularly important at higher charge/discharge rates. Fast, near-surface Faradaic reactions (also referred to as pseudocapacitive processes) can improve charge storage for rapid charge/discharge, which has been most extensively studied for RuO_2 in aqueous electrolytes and has since been shown for anodes in LIBs for various nano-sized TiO_2 polymorphs (anatase [14], Nb-doped anatase [15], Mo-doped anatase [16], TiO_2(B) [17], and TiO_2 bronze[18]) as well as for nano-sized MoO_2 [12].

Molybdenum dioxide has been used in anodes for LIBs both as an intercalation material[19] and as a conversion-type anode [20–25]. As intercalation material, MoO_2 has a theoretical specific capacity of 209 mAh g^{-1} [26] and as a conversion material (when cycled to potentials below 1.0 V vs. Li/Li^+) the theoretical specific capacity is 838 mAh g^{-1} [27]. Due to this and the comparatively high abundance and low cost of molybdenum, MoO_2 is of interest as active material for negative electrodes in energy storage devices.[28] However, MoO_2 suffers from dramatic capacity fading when cycled as a conversion anode due to the gradual deterioration of electrode integrity.[29] Ways of increasing the cycling stability of conversion electrode materials include the incorporation of more stable inorganic phases that do not undergo large volume or structural changes [30,31] such as TiO_2, due to its structural and chemical stability [32–34]. Alternatively, nano-sizing of MoO_2 or the use of carbon coatings have been investigated to overcome some of the limitations of MoO_2. Therefore, scalable methods for the fabrication of nanoceramics that allow for the incorporation of other stabilising nanomaterials or coatings to be added to active nanomaterials are desirable [12,22,35].

Synthesis processes for making nanomaterials and composites are often limited in terms of their scalability [35]. Synthesis processes for MoO_2 nanoparticles may involve multi-step processes (resulting in variations in particle properties) [36], involve long reaction times [37], or require multiple energy intensive annealing or processing steps [38]. In contrast to batch or multi-step processes,

continuous processes can offer advantages such as directly forming products and more precise control over reaction conditions during nucleation and growth of nanoparticles.

Specifically, highly scalable continuous hydrothermal flow synthesis (CHFS) methods can be used to reproducibly manufacture crystalline nanomaterials [39–41]. In CHFS processes, a feed of supercritical water (typically at 450 °C) is brought in contact with an ambient temperature aqueous solution of metal salt(s) in a well-defined mixer to bring about the instantaneous formation of nanoparticle metal oxides via reactions that include hydrolysis and dehydration [42]. In such flow processes, "ready to use" crystalline nanoparticles can be harvested from the end of the flow process as a water-dispersed slurry at ambient temperatures (see experimental section).

Herein, we describe the direct synthesis of both ultrafine MoO_2 and composite TiO_2/MoO_2 nanoparticles using a CHFS process. The CHFS-made TiO_2/MoO_2 nanocomposite-containing anodes showed significantly improved cycling stability in a Li-ion half-cell compared to the analogous MoO_2 nanoparticles.

2. EXPERIMENTAL SECTION

2.1. Synthesis

The synthesis of phase-pure anatase TiO_2 via CHFS has been described elsewhere by the authors [15,16]. Herein, MoO_2 nanoparticles and a TiO_2/MoO_2 nanocomposite material were synthesized using a (lab-scale) CHFS process, the basic design of which has been described at both lab-scale [43] and pilot scale (current capacity up to ca. 2 kg h^{-1}) [44]. Critical to the continuous production of nanoparticles in flow via the CHFS process is the patented (co-current) Confined Jet Mixer (CJM) [45] made from off-the-shelf Swagelok™ parts. The CJ mixer under these conditions facilitates highly efficient (turbulent) mixing of a low-density supercritical water stream with a denser ambient temperature aqueous metal salt solution stream. In the CHFS process of the authors, three Primeroyal K diaphragm pumps (Milton Roy, Pont-Saint-Pierre, France, pressurized to 24.1 MPa) were used to supply the three process feeds; first, DI water (10 MΩ) was supplied by Pump 1 and heated in flow to above its critical point (T_c = 374 °C and P_c = 22.1 MPa) to a temperature of 450 °C using a custom-made in-line 7 kW electrical water heater. Pump 2 was used to supply the aqueous mixture of metal salt(s) and Pump 3 supplied DI water. Feeds 2 and 3 were first combined in flow in a dead-volume Tee-piece at room temperature, before mixing with the superheated DI water feed (pumped from Pump 1) in the CJM (under highly turbulent conditions; with a Reynolds number of ca. 6000).

The metal salt precursors used were TiBALD [titanium(IV) bis(ammonium lactato)dihydroxide solution, 50 wt.% in H_2O, Sigma-Aldrich, Steinheim, Germany], ammonium molybdate tetrahydrate (99.98 %, Sigma-Aldrich, Steinheim, Germany), and L-ascorbic acid (99 %, Sigma-Aldrich, Steinheim, Germany). Before use, an aqueous solution of the molybdenum (6+) salt was stirred vigorously for ten minutes with ascorbic acid as reducing agent, using a magnetic stirrer, to reduce Mo^{6+} to Mo^{4+}, as indicated by a change in colour of the solution from yellow to dark blue.

For the synthesis of TiO_2/MoO_2 in a molar ratio of 1:4, Pump 2 supplied a feed of 0.4 M $[(NH_4)_6Mo_7O_{24}\cdot 4H_2O]$, 0.4 M $C_6H_8O_6$ and 0.1 M TiBALD. For the synthesis of MoO_2, Pump 2 supplied a feed of 0.3 M $[(NH_4)_6Mo_7O_{24}\cdot 4H_2O]$ and 0.3 M $C_6H_8O_6$.

The mixing of the aforementioned feed flows in the CJM led to the rapid formation of nanoparticles in flow, and after a residence time of ca. 5 s, a 1 m pipe-in-pipe counter-current cooler (heat exchanger) was used to chill the aqueous stream of very hot nanoparticles to ca. 40 °C.

Thereafter, the nanoparticle-laden slurry passed through a back-pressure regulator at the end of the CHFS process to be collected in a beaker. The particles were cleaned by dialysis in DI water for 48 h before being freeze-dried (Virtis Genesis 35XL) via cooling to -40 °C under vacuum of 13.3 Pa and subsequent heating to room temperature over the course of 22 h. All powders were used as-prepared thereafter.

2.2. Physical characterization

Powder X-ray diffraction (PXRD) was performed to collect diffraction patterns in a 2θ range from 10 to 40° using Mo-Kα radiation (λ = 0.7107 Å), with a step size of 0.5°, and a step time of 20 s, on a STOE StadiP diffractometer.

High-resolution transmission electron microscopy (TEM) using a JEOL JEM 2100 – LaB_6 filament was used to determine size, interlayer spacing and particle morphology. A Gatan Orius digital camera was used for image capture of the samples that were pipetted on a 300-mesh copper film grid (Agar Scientific, Stansted, UK). Energy dispersive X-ray spectroscopy (EDS) was also performed using the JEOL JEM 2100 for elemental analysis of the samples.

The valence states of the metal ions were determined using X-ray photoelectron spectroscopy (XPS) collected on a Thermo Scientific K-alpha™ spectrometer using Al-Kα radiation equipped with a 128-channel position sensitive detector. High-resolution regional scans for molybdenum were conducted at 50 eV. Processing of the XPS data was performed using CasaXPS™ software (version 2.3.16) and by calibrating the spectra using the C 1s peak at 284.8 eV.

Brunauer-Emmett-Teller (BET) surface area measurements were carried out using liquid N_2 on a Micrometrics Tristar II. The samples were degassed at 150 °C (12 h) using Ar gas before measurements were undertaken.

Field emission scanning electron microscopy (FE-SEM) was carried out using a JEOL JSM-6700F microscope operating with an accelerating voltage of 5 kV to study the surfaces of electrodes after cycling.

The tap densities of the nanomaterials were determined by measuring ca. 1.5 g of powder into a graduated cylinder and manually tapping it vertically on a benchtop 300 times.

2.3. Electrochemical characterization in half-cells

Anodes were prepared by mixing of CHFS-made MoO_2 active material with a polymeric binder (polyvinylidene fluoride, PVDF, PI-KEM, Staffordshire, UK) and a conductive carbon (Super P, Alfa Aesar, Heysham, UK) in a ratio of 80:10:10 wt.%. The PVDF was added as a pre-mixed 10 wt.% solution of PVDF in N-methyl-2-pyrrolidone (NMP, Sigma Aldrich, St. Louis, USA). The solution was mixed manually with the active material and the conductive carbon and further NMP (ca. 2.5 mL) was added to give a viscous slurry. The slurry was ball-milled at 800 rpm for 1 hour before being cast on 9 μm copper foil (PI-KEM, Staffordshire, UK) as the current collector. The electrode sheets were dried on a hotplate at ca. 150 °C for 20 minutes until superficially dry and then left to continue drying overnight at room temperature. All electrodes were dried overnight under vacuum at 40 °C before being introduced into an Ar-filled glovebox (H_2O and O_2 < 5 ppm) for cell assembly. The active mass loading of the anodes was in the range 1.8 to 2.0 mg cm^{-2}.

Half-cell tests were performed using CR2032 coin cells. Whatman GF/D glass microfiber filters (Buckinghamshire, UK) were used as the separator and drenched in an organic electrolyte (1 M $LiPF_6$ in 1:1 volume ratio ethylene carbonate/ethyl methyl carbonate, BASF, Ludwigshafen,

Germany). For the half-cells, lithium metal foil (PI-KEM, Staffordshire, UK) was used as the counter electrode. Li-ion battery electrodes with TiO_2/MoO_2 or MoO_2 as the active component were tested using cyclic voltammetry in the potential window 0.1 to 3.0 V vs. Li/Li^+ at scan rates in the range 0.1 to 100 mV s^{-1}. The half-cell galvanostatic charge/discharge cycling was carried out using an Arbin Instrument Model BT-2000 battery tester (Caltest Instruments Ltd, Guildford, UK) at room temperature. The tests were carried out in the potential range 0.1 to 3.0 V vs. Li/Li^+ at specific currents in the range 0.1 to 15.0 A g^{-1}. Cyclic voltammetries (CVs) for the half-cells were recorded in the potential window 0.1 to 3.0 V vs. Li/Li^+, at scan rates in the range 0.1 to 100.0 mV s^{-1}.

Galvanostatic electrochemical impedance spectroscopy (EIS) was performed on a Gamry Interface 1000 instrument (Gamry Instruments, Pennsylvania, US). The AC current was set to 0.01 A rms. The frequency range was 100 kHz to 50 mHz.

Staircase potentio electrochemical impedance spectroscopy (SPEIS) was performed on Swagelok-type half-cells using a Bio-Logic VS.P-300 potentiostat (Bio-Logic Science Instruments, Seyssinet-Pariset, France) in the potential window 0.1 to 3.0 V vs. Li/Li^+ with a potential of 0.01 V rms in the frequency range 100 kHz to 10 mHz. Each potential step was held until the measured current had relaxed to below 1 mA.

2.4. Electrochemical characterization in Li-ion hybrid electrochemical capacitors

Anodes cut from the same sheet as those used for testing in Li-ion half-cells were used in Li-ion hybrid electrochemical capacitors (Li-HECs), due to their excellent performance at high applied currents in Li-ion half-cells. Activated carbon (AC) electrodes were used as cathodes. The preparation of the AC electrodes has previously been described elsewhere. In brief, they were prepared by mixing 87 wt.% activated carbon active material (YP50F, Kuraray Chemical Co., Osaka, Japan) with 8 wt.% of a binder (PVDF) and 5 wt.% carbon black (SuperP^{TM}) and casting on a Megtec reel-to-reel coater on aluminium foil.[16]

Electrochemical tests for the Li-HECs were performed in two-electrode Swagelok-type cells that were assembled in an Ar-filled glovebox with O_2 and H_2O < 5 ppm. Whatman GF/D glass microfiber filters (Buckinghamshire, UK) drenched in an organic electrolyte (1 M $LiPF_6$ in 1:1 volume ratio of ethylene carbonate/ethyl methyl carbonate, BASF, Ludwigshafen, Germany) were used as separators. The mass ratio between active material in anode and cathode was not optimized, and kept in line with previous work at a mass ratio of ca 2:7.[16]

Cyclic charge/discharge measurements and CVs for the Li-HECs were performed on a Gamry Interface 1000 instrument (Gamry Instruments, Pennsylvania, US). Galvanostatic charge/discharge cycling was performed at current densities in the range of 2.0 to 20.0 mA cm^{-2}, based on the geometric surface area of the electrodes, in the potential window of 1.0 to 3.0 V. This was equivalent to specific currents based on the mass of active materials in both electrodes of ca. 0.3 to 3.0 A g^{-1}. The CVs were performed at scan rates in the range 5 to 100 mV s^{-1} in the potential window 1.0 to 3.0 V.

3. RESULTS AND DISCUSSION

Well-dispersed dark slurries of nanoparticles were obtained, which settled overnight (after the addition of ca. 50 g of NaCl per litre of dispersion). The supernatant was removed, and the black wet solids were dialysed in DI water. After dialysis and freeze-drying, the nanoparticles were recovered as shiny black powders. Due to the high stability of the dispersions and small particle sizes, there were some losses during clean-up, which were higher for the pure MoO_2 sample. A yield of > 90% was

recorded for the composite sample, which meant a production process rate of > 85 g per hour. Both samples were black in colour and shiny.

Powder XRD revealed well-defined peaks for both samples (see Figure 1a) that were a good match to the standard reference pattern for tugarinovite MoO_2 (JCPDS reference card no. 078-1073, space group $P2_{i/c}$). The major peaks for both samples corresponded to the (011), (-211) and (-311) peaks for MoO_2 (2θ = 11.9, 16.7 and 23.9 °, respectively). The XRD data for the TiO_2/MoO_2 composite showed an additional shoulder to the left of the major peak at 2θ = 11.6 °, corresponding to the (101) peak of anatase TiO_2. There was also an additional peak at 2θ = 21.6° corresponding to the (200) peak of anatase. Scherrer equation calculations for the major peaks in both samples yielded estimated crystallite sizes of 16.4 nm for MoO_2 in the pure sample and 11.3 nm for MoO_2 in the composite. Crystallite size analysis on the deconvoluted shoulder of the peak for TiO_2 gave an estimated crystallite size of ca. 5 nm.

The valence states of titanium and molybdenum ions in both the TiO_2/MoO_2 composite and MoO_2 were determined using high-resolution X-ray photoelectron spectroscopy (XPS). The Ti 2p level binding energies for the TiO_2/MoO_2 composite were at 459.1 and 465.0 eV for Ti $2p_{3/2}$ and Ti $2p_{1/2}$, respectively. This gave a spin-orbit splitting of 5.9 eV that could be ascribed to the core level of Ti^{4+}. A comparison of Ti2p peaks showed little difference between the Ti^{4+} species found in the composite compared to that in pure TiO_2 [16]. For Mo ions, three distinct peaks were observed at 229.6, 232.8 and 236.0 eV, which were ascribed to a mixture of Mo^{4+}, Mo^{5+} and Mo^{6+} valence state in the samples (see b and c). This was most likely due to surface oxidation of Mo^{4+} in the $Mo^{4+}O_2^{2-}$ to a surface layer of different molybdenum oxides, such as Mo_2O_5 and MoO_3, as has previously been observed [46,47].

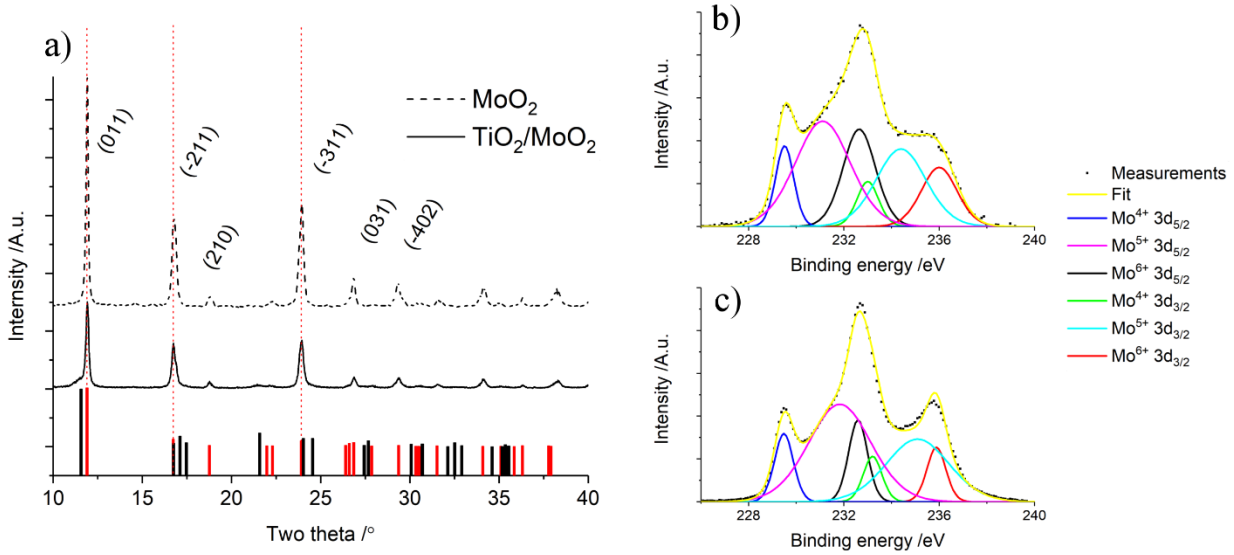

Figure 1: a) Powder X-ray diffraction (PXRD) patterns for both TiO_2/MoO_2 and MoO_2 with reference patterns for MoO_2 (tugarinovite, JCPDS card no. 078-1073) marked by red columns and TiO_2 (anatase, JCPDS card no. 071-1167) marked by black columns. High-resolution X-ray photoelectron spectroscopy (XPS) for Mo3d for both the composite b) TiO_2/MoO_2 and c) MoO_2.

Semi-quantitative analysis of the XPS peak areas for the TiO_2/MoO_2 composite suggested an estimated elemental composition of ca. 60 at.% titanium, which indicated a strongly enriched loading

of TiO_2 on the surface. Hence, TiO_2 nanoparticles may have been concentrated on the surface of MoO_2 nanoparticles in the composite sample.

EDS analysis revealed an even distribution of titanium ions throughout the TiO_2/MoO_2 composite (see Figure 2a-d). This homogeneity was contrasted by the distribution of Mo ions, which did not appear to be as homogenously distributed. Parts of the sample showed high molybdenum ion concentration, some equal concentrations of Ti and Mo ions and some no molybdenum ions. This pointed to the elements forming separate phases. This suggested either very different rates of hydrolysis or low solid solution solubility of the products. Elemental analysis of several large agglomerates of composite material using EDS showed (on average) good agreement with the original Ti:Mo molar ratio used in the synthesis, indicating a value of 21 ± 2 at.% titanium.

Transmission electron microscopy revealed small spherical particles for both samples (Figure 3a and 3c). TEM images suggested an average particle size (150 particles counted) of 18.9 ± 6.2 nm for MoO_2 compared to 9.1 ± 5.9 nm for the TiO_2/MoO_2 composite (see Figure 2e and 2f). The interlayer spacings for both samples were determined using lattice fringes visible from TEM images, such as shown in Figure 3b and 3d. Two different interlayer spacings of 0.24 and 0.34 nm were observed for both samples that corresponded to the (-211) and (011) interlayer spacings, respectively, of monoclinic MoO_2 [48].

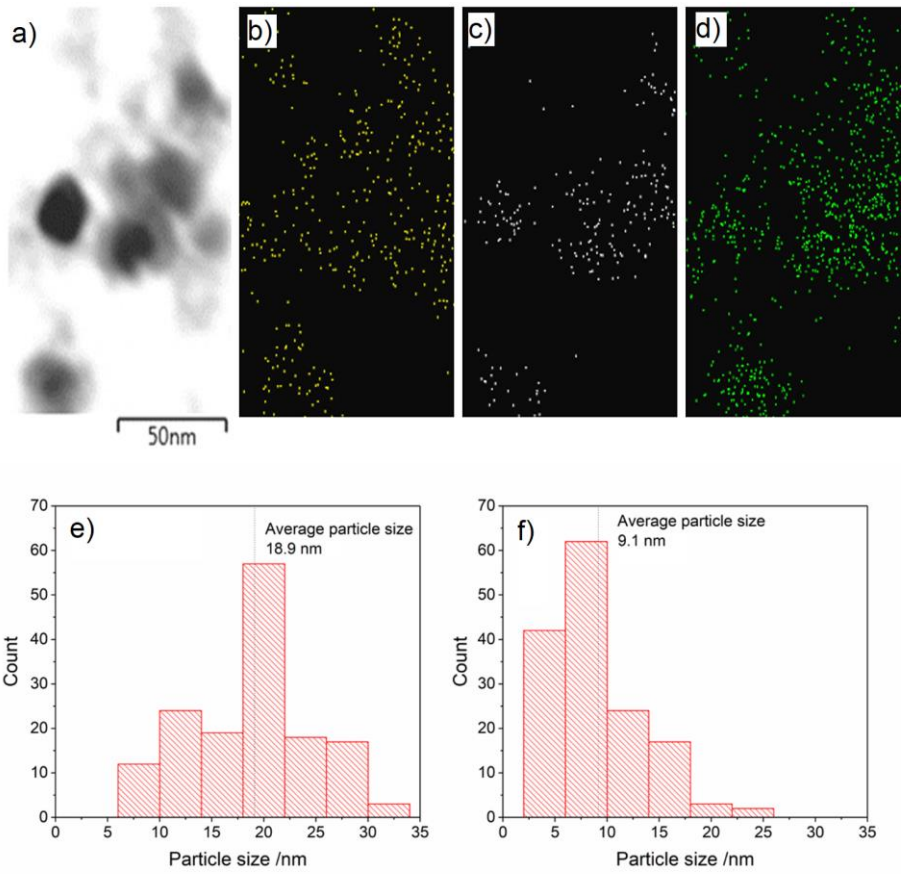

Figure 2: a) Scanning transition electron microscopy (STEM) dark-field image showing the TiO_2/MoO_2 composite and energy-dispersive X-ray spectroscopy (EDS) maps for b) Ti (yellow), c) Mo (grey), and O (green). Histograms showing the particle sizes of 150 particles for both e) the MoO_2 sample and f) the TiO_2/MoO_2 composite.

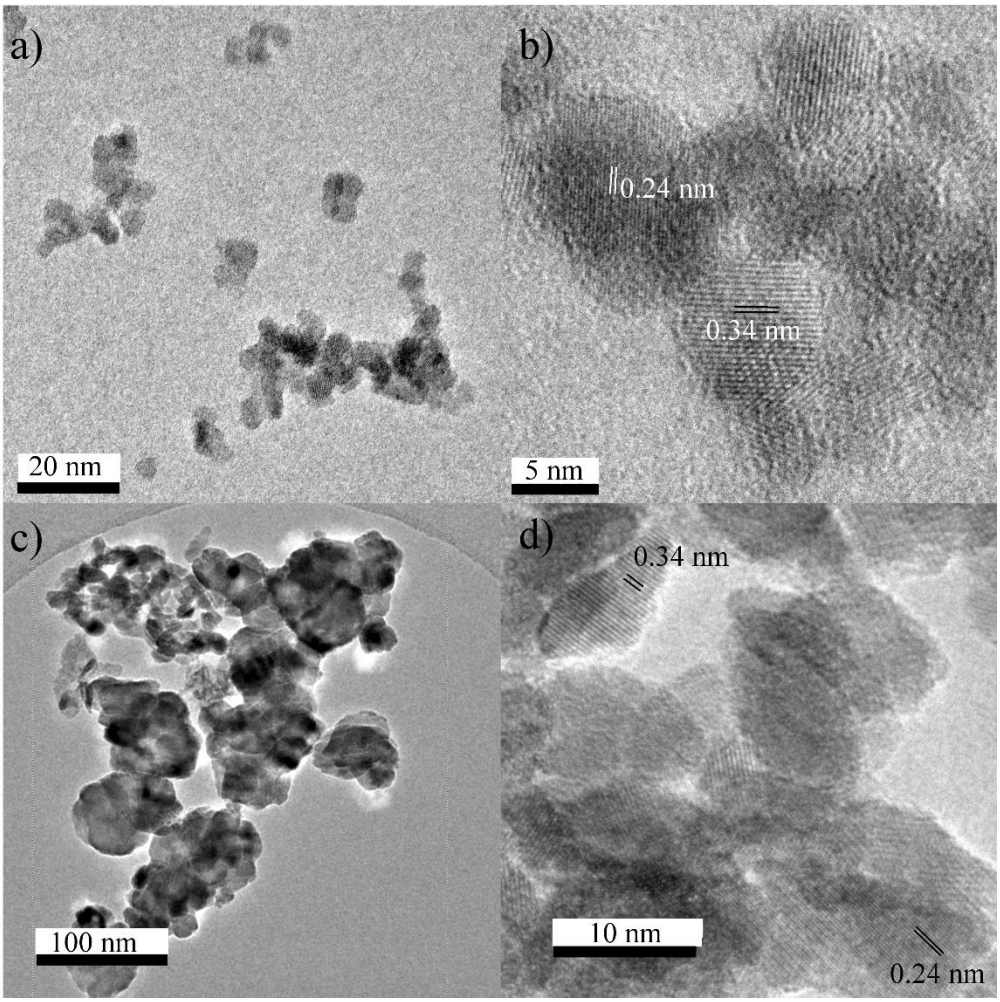

Figure 3: Transmission electron microscopy (TEM) images showing the a) TiO_2/MoO_2 composite and the interlayer spacing of b) the TiO_2/MoO_2 composite. TEM image showing the particle size and morphology of c) the MoO_2 particles as well as an image showing the interlayer spacing of 0.24 and 0.34 nm for the d) MoO_2 are also shown.

The BET surface areas for the MoO_2 and TiO_2/MoO_2 samples were ca. 21 and 105 $m^2\ g^{-1}$, respectively. Pure TiO_2 synthesised via CHFS has been shown to possess a specific surface area of ca. 280 $m^2\ g^{-1}$ [49], so even assuming separate formation of 20 mol% TiO_2 and 80 mol% MoO_2 particles (equal to 14 wt.% TiO_2 and 86 wt.% MoO_2), the surface area of MoO_2 particles in the composite was affected by the presence of Ti salt.

The tap density of the as-synthesised MoO_2 was 0.92 g cm^{-3}, whereas that of the TiO_2/MoO_2 composite was 1.54 g cm^{-3}. This significant increase in tap density was possibly a result of the decreased particle size and better packing of the composite sample.

The results from potentiodynamic tests for the composite and MoO_2 cells are shown in Figure 4a and 4b, respectively (at scan rates of 0.1, 0.2, 0.5 and 1.0 mV s^{-1}). The plots for the composite material at 0.1 mV s^{-1} showed three distinct anodic peaks (Li^+ extraction) at ca. 1.4, 1.7 and 2.1 V vs. Li/Li^+ and two major cathodic (Li^+ insertion) peaks at 1.25 and 1.5 V vs. Li/Li^+ and one minor peak at 1.8 V vs. Li/Li^+. The two oxidation peaks at 1.4 and 1.7 V vs. Li/Li^+ can be ascribed to the phase transitions from monoclinic to orthorhombic and back to monoclinic phase as Li^+ was extracted from

MoO_2, as previously described in the literature [19,20]. The reactions of MoO_2 in the potential range 1.0 to 3.0 V vs. Li/Li^+ can therefore be described by Equation (1):

$$MoO_{2\,(monoclinic)} \rightleftharpoons Li_xMoO_{2\,(0.45<x<0.78,orthorombic)} \rightleftharpoons Li_{0.98}MoO_{2\,(monoclinic)} \quad (1)$$

Cycling to lower potential such as 0.1 V vs. Li/Li^+ subsequently resulted in the partial conversion reaction of the fully lithiated $Li_{0.98}MoO_2$ to molybdenum metal and lithium oxide, as per Equation (2) [27,38,50]:

$$Li_{0.98}MoO_{2\,(monoclinic)} + 3.02\ Li^+ + 3.02\ e^- \rightleftharpoons 2Li_2O + Mo \quad (2)$$

The additional extraction peak at 2.1 V vs. Li/Li^+ and additional insertion peak at 1.8 V vs. Li/Li^+ observed in the cyclic voltammogram of the composite sample could be ascribed to the Ti^{3+}/Ti^{4+} transition in TiO_2 [15,16]. As the scan rate increased, the separation between anodic and cathodic peaks increased due to polarization of the electrodes. At a scan rate of 1 mV s^{-1}, the third oxidation peak for the Ti^{3+}/Ti^{4+} transition almost disappeared, whilst the two extraction peaks for MoO_2 were still very distinct.

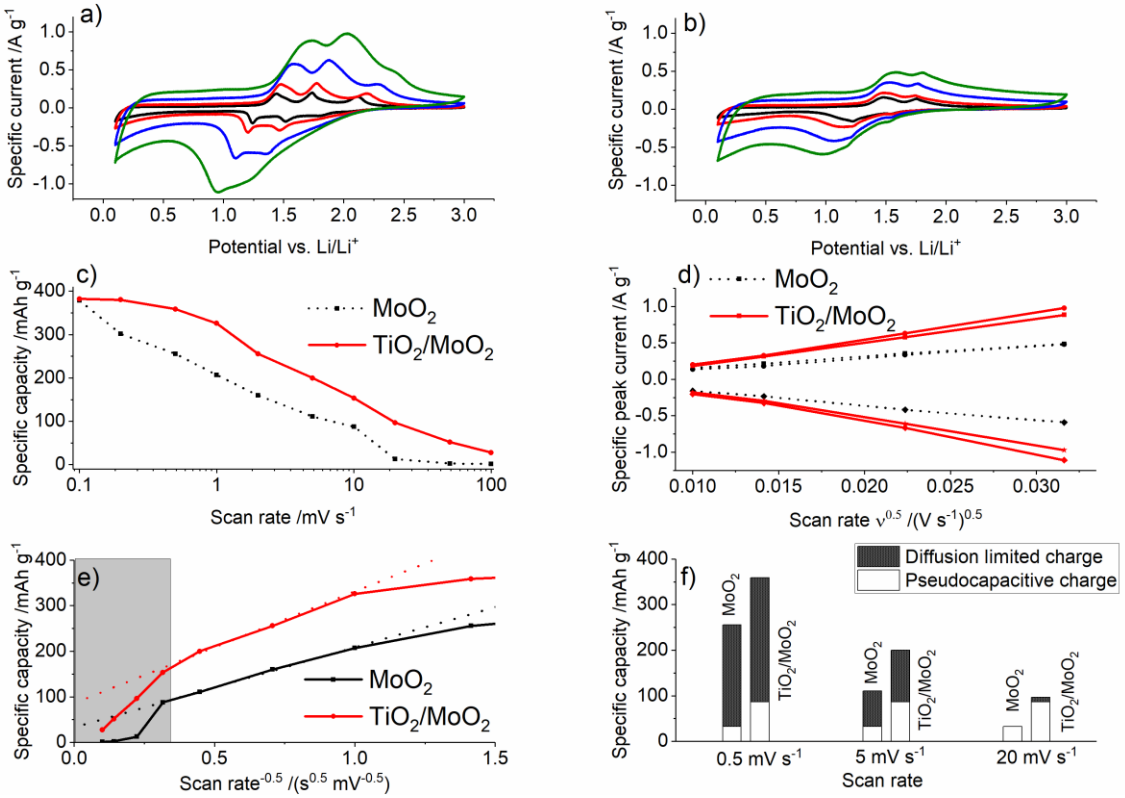

Figure 4: Cyclic voltammograms for a) TiO_2/MoO_2 composite and b) MoO_2 at 0.1, 0.2, 0.5 and 1.0 mV s^{-1} in black, red, blue and green, respectively. c) Plots of specific capacities over scan rate for both. d) The relationship between specific peak currents and scan rate. e) Plots of specific capacity over the reciprocal of the square root of the scan rate (with high scan rate region in grey excluded from analysis) and f) proportion of pseudocapacitive charge storage for both the composite and pure MoO_2 at 0.5, 5 and 20 mV s^{-1} are also shown.

The half-cells using electrodes with MoO_2 as active material showed only the two Li-ion extraction peaks for MoO_2. These were at similar potentials to those observed for the composite sample, at ca. 1.4 and 1.7 V vs. Li/Li^+ (at a scan rate of 0.1 mV s^{-1}). An increase in scan rate, however, resulted in a much smaller increase in current for the pure MoO_2 sample, and the peaks became less distinct. This indicated more sluggish Li-ion diffusion at high rates for this sample compared to the nanocomposite. This was confirmed by the increased capacity retention for the composite sample at higher scan rates (see Figure 4c). The relationship between specific peak current and scan rate for the intercalation peaks of MoO_2 was plotted in Figure 4d. Both anodic and cathodic peak currents were higher at each scan rate for the composite sample, compared to pure MoO_2. The Randles-Sevcik equation [51–53] (Equation 3) was used to calculate the apparent diffusion coefficients.

$$I_p = 2.69 \times 10^5 n^{\frac{3}{2}} A D^{\frac{1}{2}} C v^{\frac{1}{2}} \quad (3)$$

In Equation 3, the peak current (I_p) is related to the number of electrons involved in the intercalation (n), the surface area of the electrode (A), the concentration of Li^+ (C), the scan rate (v) and the diffusion coefficient (D).

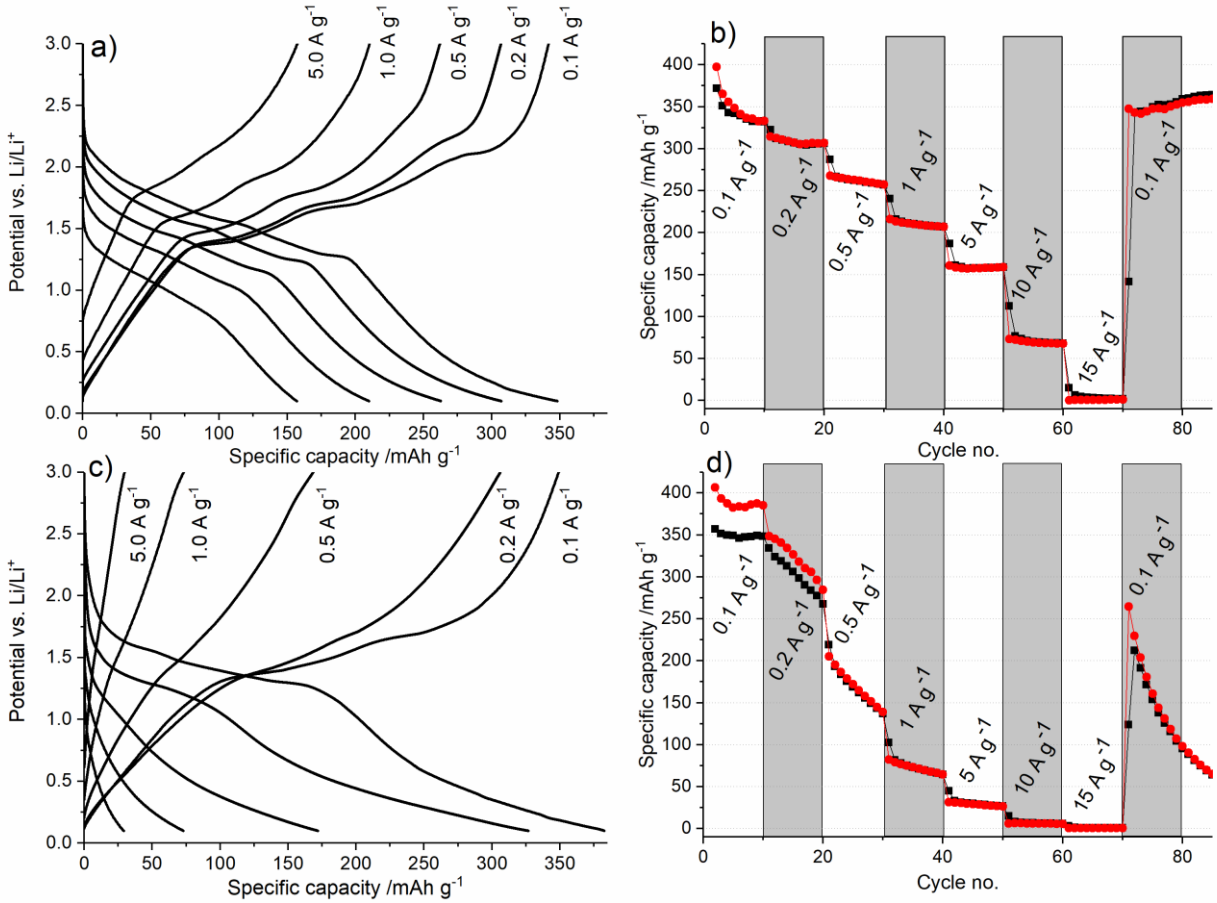

Figure 5: Charge/discharge curves for the 5th cycle for a) TiO_2/MoO_2 and c) MoO_2 at specific currents of 0.1, 0.2, 0.5, 1, and 5 A g^{-1}; as well as C-rate cycling data for b) TiO_2/MoO_2 and d) MoO_2, with both charge (red) and discharge (black) capacities shown.

The specific diffusion coefficients for the pure MoO_2 sample were ca. 1.0×10^{-9} (anodic) and 1.3×10^{-9} cm^2 s^{-1} g^{-1} (cathodic), whereas the diffusion coefficients for the composite TiO_2/MoO_2

sample were significantly higher (ca. 2.8×10^{-9} and 3.0×10^{-9} cm^2 s^{-1} g^{-1} for anodic and cathodic redox processes, respectively). The contributions of both near-surface (fast Faradaic and minor double layer charge storage) processes and intercalation to the specific current were estimated using Equations 4, 5 and 6 [9,54,55].

The total current q_T can be expressed by Equation 4:

$$q_T = q_s + q_d \quad (4)$$

Where q_s is the charge related to fast pseudocapacitive charge storage and q_d the charge due to slower diffusion-limited processes.

The pseudocapacitive contribution to charge storage (PCS) can therefore be calculated using Equation (5), and because the diffusion-controlled behaviour is linearly related to $v^{-0.5}$, Equation 4 can be rewritten as Equation 6:

$$PCS = q_s/q_T \quad (5)$$

$$q_T = q_s + cv^{-0.5} \quad (6)$$

The specific capacity was plotted versus reciprocal square root of the scan rate ($v^{-0.5}$) inFigure 4e. The pseudocapacitive contributions to charge storage were calculated to be ca. 24 % at 0.5 mV s^{-1} for the composite sample, but only ca. 13 % for the pure MoO_2 (see Figure 4f). At a higher scan rate of 5 mV s^{-1} the PCS contributions were ca. 43 and 30 % for TiO_2/MoO_2 and MoO_2, respectively. Finally, at 20 mV s^{-1}, pseudocapacitive charge storage contributions were nearly 100 % for both samples; calculated pseudocapacitive charge stored at a theoretical, infinitely fast scan rate was 311 C g^{-1} for TiO_2/MoO_2, but only 119 C g^{-1} for MoO_2. These values were comparable to those previously reported in the literature for nanosized MoO_2 (values reported for nanosized were 300 C g^{-1} at 10 mV s^{-1}) [12]. Herein, the larger contribution of pseudocapacitive charge storage in the composite sample was attributed to the smaller size of the MoO_2 particles in the composite (versus the pure MoO_2 material), which facilitated enhanced fast near-surface charge storage processes [56].

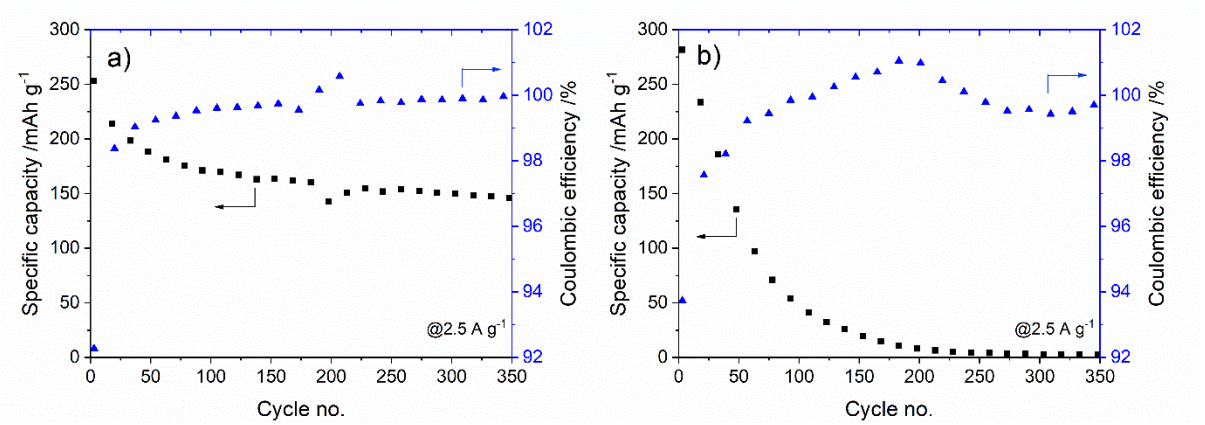

Figure 6: Specific capacities for a) TiO_2/MoO_2 and b) MoO_2 at a constant specific current of 2.5 A g^{-1}.

These findings were supported by the results of galvanostatic charge/discharge measurements (see Figure 5a and 5c) at specific currents of 0.1, 0.2, 0.5, 1, 5, 10 and 15 A g^{-1}, in the potential window of 0.1 to 3.0 V vs. Li/Li^+. The charge/discharge curves for half-cells with TiO_2/MoO_2 electrodes at lower currents (e.g. 0.1 A g^{-1}) showed three separate plateaus. The two plateaus at lower potentials vs. Li/Li^+ corresponded to phase transformation from monoclinic $Li_{0.98}MoO_2$ to orthorhombic Li_xMoO_2 ($0.45 < x < 0.78$) and back to monoclinic MoO_2 [19], as observed from peaks in the cyclic voltammograms.

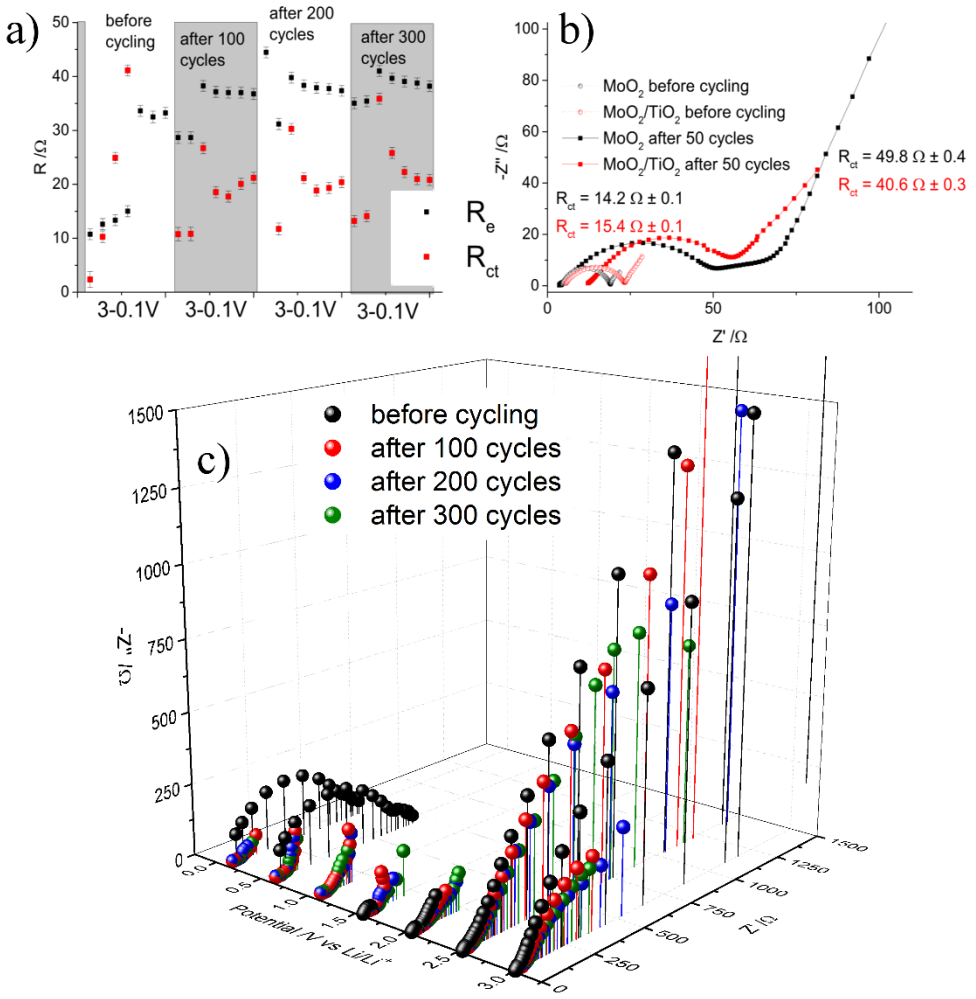

Figure 7: a) Development of the electronic resistance (R_e) and charge transfer resistance (R_{ct}) during staircase potentio electrochemical impedance spectroscopy (SPEIS) in the potential range 3.0 to 0.1 V vs. Li/Li^+ before and after cycling. b) EIS of half-cells is shown in electrodes using MoO_2 (black) and the TiO_2/MoO_2 composite (red) as active material both before (spheres) and after (squares) cycling. c) Nyquist plots at various potentials before cycling and after 100, 200 and 300 cycles.

The plateau at ca 2.0 V vs. Li/Li^+ was due to lithium extraction from the anatase lattice of the TiO_2 [14]. This assignment was supported by the observation that no corresponding plateau was found in the charge/discharge profile for the half-cells with anodes made of pure MoO_2.

Current rate testing revealed similar initial specific discharge capacities for both samples at low applied currents (ca. 350 mAh g^{-1} at 0.1 A g^{-1} after 10 cycles), but there were significant differences at higher specific currents (see Figure 5b and 5d). TiO_2/MoO_2 showed superior capacity retention and rate behaviour as well as higher Coulombic efficiencies in the first twenty cycles (at lower applied currents). An increase in the applied specific current to 0.2 A g^{-1} led to a significant reduction in specific capacity for the pure MoO_2-based electrodes and noticeable reduction in cycle life, with a loss of 25 % in capacity after 10 cycles. In comparison, at a specific current of 1 A g^{-1}, the TiO_2/MoO_2 electrodes showed a stable specific discharge capacity of ca. 225 mAh g^{-1}; under these conditions, MoO_2 showed a steadily decreasing specific discharge capacity < 100 mAh g^{-1}. Even at specific

currents of 5 and 10 A g^{-1}, TiO_2/MoO_2 half-cells still delivered stable and high specific discharge capacities of ca. 160 and 70 mAh g^{-1}, respectively. This meant that a specific capacity of 160 mAh g^{-1} could be stored and discharged within less than 2 minutes.

When the specific current was subsequently returned to 0.1 A g^{-1} after 70 cycles at a range of specific currents (up to 15 A g^{-1}), the specific capacity of TiO_2/MoO_2 recovered to ca. 350 mAh g^{-1} and remained stable. In contrast, the pure MoO_2 was unstable, and after recovering to a specific capacity of ca. 210 mAh g^{-1}, dropped to ca. 100 mAh g^{-1} after another 10 cycles at 0.1 A g^{-1}. The improved capacity and cycling stability for the TiO_2/MoO_2 was attributed to the diluting and stabilising effect of TiO_2 particles (which underwent minimal volume changes upon cycling) on the normally relatively unstable MoO_2 conversion material when cycled below 1.0 V vs. Li/Li^+. This was in line with cycling stability tests at 2.5 A g^{-1} (see Figure 6). TiO_2/MoO_2 retained a specific capacity of ca. 150 mAh g^{-1} after 350 cycles; the pure MoO_2 could not retain any discharge capacity after 200 cycles. (and < 100 mAh g^{-1} after 70 cycles). Pure TiO_2 synthesised via the same CHFS process cycled in the same potential window showed significantly worse performance, with maximum specific capacities of only ca. 225 and 120 mAh g^{-1} at specific currents of 0.1 and 1 A g^{-1}, respectively [57].

TiO_2 has previously been used in composite electrodes to stabilise the Li-ion storage properties of alloying materials such as sulphur and MoS_2 [31,58,59]. In the work herein, the improved charge storage at high rates can be explained by the smaller particle size and higher surface area of the MoO_2 phase in the TiO_2/MoO_2 composite particles [56,60], which led to higher pseudocapacitive contributions and better apparent lithium-ion diffusion at high applied currents.

Staircase Potentio Electrochemical Impedance Spectroscopy (SPEIS) of half-cells using anodes made from TiO_2/MoO_2 composite revealed that at a potential of 3.0 V vs. Li/Li^+ (fully discharged state), the Nyquist profile changed significantly after cycling. Both charge transfer resistance and solution resistance were largely consistent after cycling, revealing similar Nyquist plots after 100, 200 and 300 cycles. At 2.0 V vs. Li/Li^+, the Nyquist plots after 100, 200, and 300 cycles remained consistent but was significantly different to the Nyquist plot before cycling. Due to electrolyte decomposition, the solution resistance (R_e) was significantly higher after cycling than it was before, both at 3.0 and 2.0 V vs. Li/Li^+.

The maximum charge transfer resistances (R_{ct}) were observed at a potential of 2.0 V vs. Li/Li^+ for all measurements after cycling and increased from 27 to 36 Ω after cycling for 100 and 300 cycles, respectively. For impedance measurements taken in the potential window of 1.5 to 0.1 V vs. Li/Li^+, charge transfer and solution resistances did not differ significantly with different potentials and cycles. The general trend in charge transfer resistance was to increase as the cut-off potential of 0.1 V vs. Li/Li^+ was approached (see Figure 7a). The resistance due to solid electrolyte interphase formation R_{SEI} showed no clear pattern and remained between 11 and 20 Ω after 100, 200 and 300 cycles.

At open circuit voltage, the Nyquist plots (see Figure 7b) suggested that the pure MoO_2 sample had lower charge transfer and lower total impedance before cycling, compared to the TiO_2/MoO_2 composite; this was expected considering the near-metallic conductivity of crystalline MoO_2 [20] compared to the relatively poor conductivity of TiO_2 [14] and the additional phase boundaries in the composite material. However, after 40 cycles at a current rate of 0.1 A g^{-1}, the composite electrodes showed a smaller increase in charge transfer resistance. The Nyquist plots for pure MoO_2 electrodes also showed clear evidence for the presence of a second phase at OCV after cycling with an indented semicircle in the Nyquist plot in the range 50 to 70 Ω that was not observed in the corresponding plot for the composite electrode. The previously described stability of the composite electrode was also

observed via SPEIS (Figure 7: a) Development of the electronic **resistance (R_e) and charge transfer resistance (R_{ct}) during staircase potentio electrochemical impedance spectroscopy (SPEIS) in the potential range 3.0 to 0.1 V vs. Li/Li$^+$ before and after cycling. b) EIS of half-cells is shown in electrodes using MoO_2 (black) and the TiO_2/MoO_2 composite (red) as active material both before (spheres) and after (squares) cycling. c) Nyquist plots at various potentials before cycling and after 100, 200 and 300 cycles.**

c) with very little difference between half-cells cycled for 100, 200 or 300 cycles. For the composite electrodes cycled at a current rate of 0.5 A g^{-1}, the capacity losses were ca. 22, 13 and 8 % of the original capacity in the ranges 0 to 100, 100 to 200 and 200 to 300 cycles, respectively.

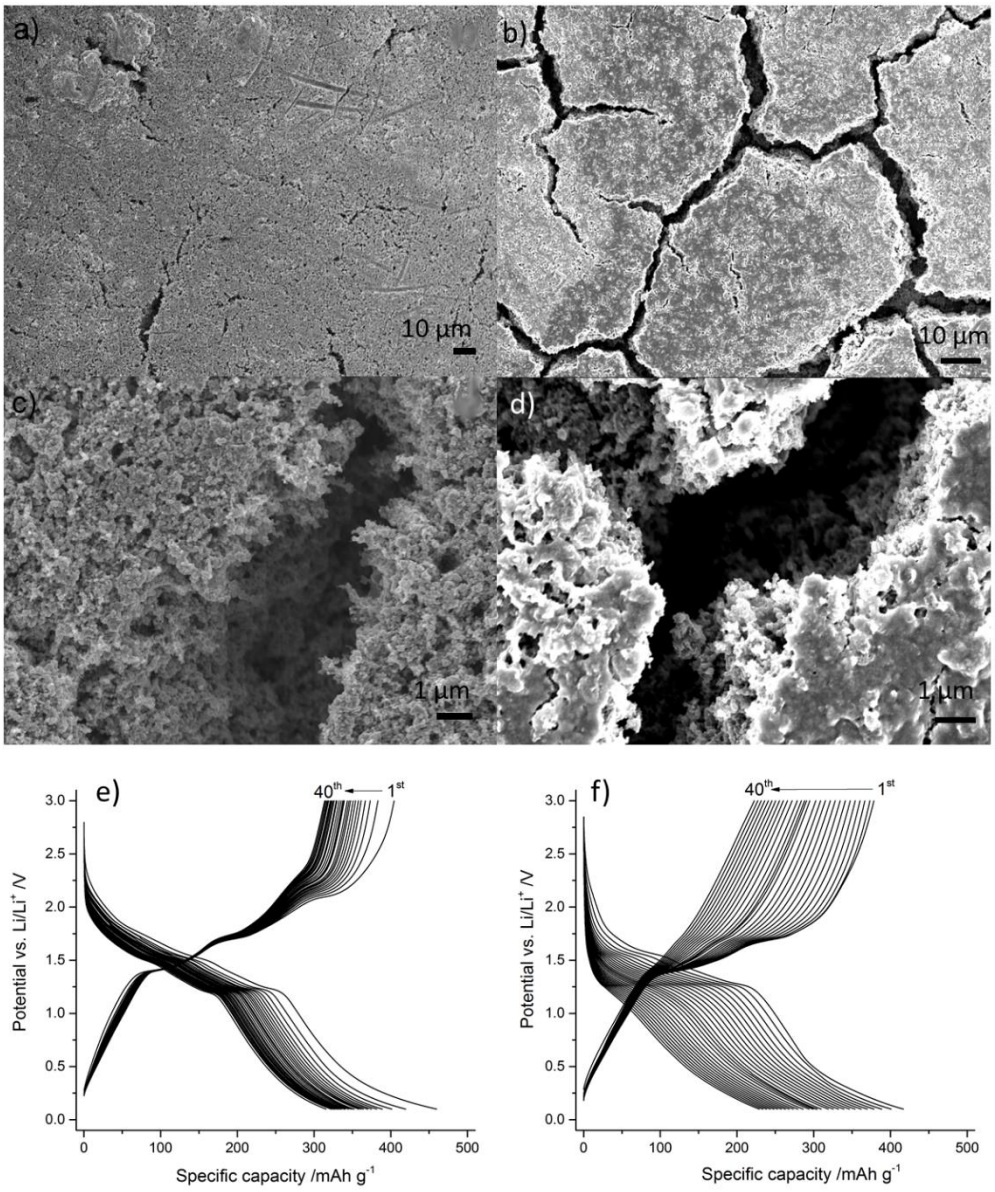

Figure 8: Scanning electron microscopy (SEM) images of electrodes made of TiO_2/MoO_2 (a, c) or MoO_2 active material (b, d) after cycling for 40 cycles. Charge/discharge cycling for TiO_2/MoO_2 (e) and MoO_2 (f) for 40 cycles at 0.2 A g^{-1}.

To explain the significantly worsening performance of the half-cells containing the pure MoO_2 electrodes, post-mortem scanning electron microscopy (SEM) was carried out. The cycled electrodes

of each material showed increased micro-cracks, which were relatively minor for the TiO_2/MoO_2 electrode (see Figure 8c), but much larger and connected for the pure MoO_2 electrode (see Figure 8d). The expansion/shrinking during lithiation and delithiation, especially during the conversion reaction, may have been responsible for cracking for each set of particles [24] and the electrode itself [61]. Due to its chemical and structural stability, TiO_2 has also been used to improve the stability of other active materials; for example, in $TiO_2@Fe_2O_3$ arrays [62], $Fe_3O_4@TiO_2$ clusters [30], and as previously mentioned a MoS_2/TiO_2 composite [59].

Because of its superior performance at high specific currents, TiO_2/MoO_2 was identified as a potential anode material for Li-ion hybrid electrochemical capacitors (Li-HECs). The cycling was limited to a potential window of 1.0 to 3.0 V to avoid lithium plating and the conversion reaction of the anode to improve cycle life. Cyclic voltammograms revealed plots similar to those previously reported for similar Li-HECs [16,63]. Visible peaks for redox reactions were fairly indistinct at the slowest scan rate of 5 mV s^{-1}, indicating good capacitor behaviour [64]. With increasing scan rate, the plots became increasingly featureless and broader (see Figure 9c). Instead, it showed a behaviour typical for a Li-HEC combining both capacitor-like and battery-like charge storage mechanisms [64–66]. During charging, fast Faradaic reactions of lithium cations with the anode and hexafluorophosphate anion absorption onto the active carbon cathodes were expected. During discharging, PF_6^- desorption and Li^+ extraction from the active material in the anode were expected [9,10,67].

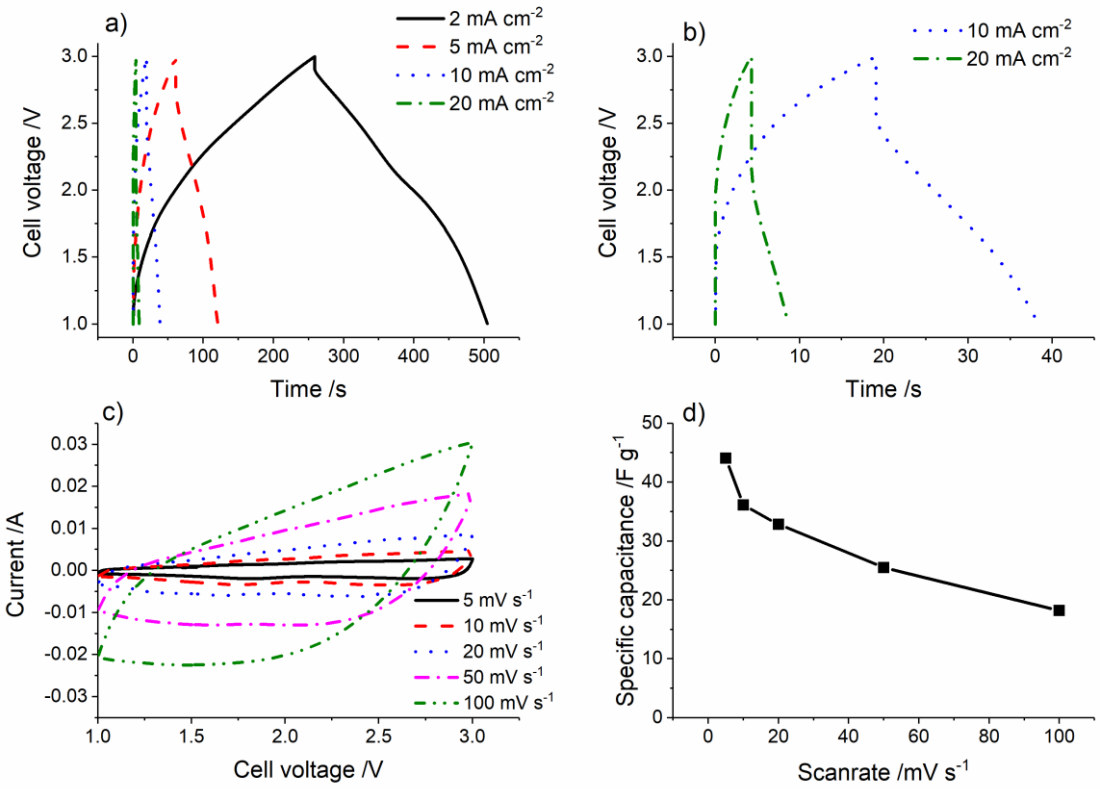

Figure 9: a) and b) Constant charge/discharge profiles for TiO_2/MoO_2//Activated carbon Li-ion hybrid electrochemical capacitors as well as c) cyclic voltammetry and d) specific capacitance of the whole cell at various scan rates.

The specific capacitance of the Li-HEC was calculated using Equation (7):

$$C_{cell} = Q/(\Delta V\, m) \quad (7)$$

Where Q was the charge (C), ΔV was the voltage change (V) and m was the mass of active material in both the anode and cathode (g). The TiO_2/MoO_2//AC Li-HEC showed specific capacitances of 44, 36, 33, 26, and 18 F g^{-1} at scan rates of 5, 10, 20, 50, and 100 mV s^{-1}, respectively (see Figure 9d).

These values were in good agreement with the results from the cyclic charge/discharge measurements, which were analysed using Equations (8) and (9):

$$C_{cell} = (I\, t)/(\Delta V\, m) \quad (8)$$

$$\Delta V = E_{max} - E_{min} \quad (9)$$

Where I was the charge current (A), t was the discharge time (s), ΔV was the potential window (V), and m was the mass of active material in both the anode and cathode (g). E_{max} and E_{min} were the potentials at the beginning and at the end of the discharge step.

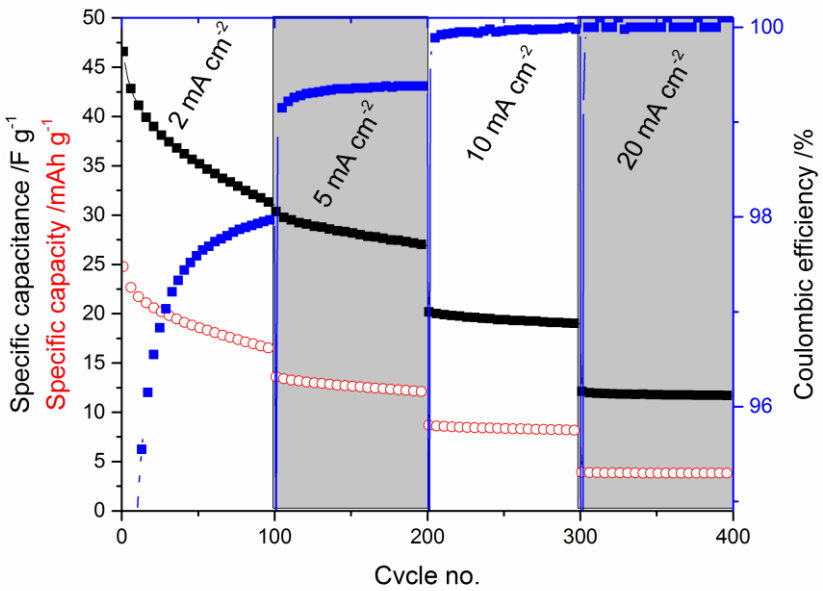

Figure 10: Cyclic charge/discharge measurements of TiO_2/MoO_2//AC Li-ion hybrid electrochemical capacitor at varying current densities.

At current densities of 2, 5, 10, and 20 mA cm^{-2}, which were equivalent to specific currents of ca. 0.3, 0.75, 1.5 and 3.0 A g^{-1} (based on the mass of active materials in both cathode and anode), respectively, the TiO_2/MoO_2//AC Li-HEC showed specific capacitances of 40, 26, 19, and 12 F g^{-1} (equivalent to specific capacities of 22, 13, 8 and 4 mAh g^{-1}), respectively. The charge/discharge curves had a nearly triangular shape, consistent with the expectations for a Li-HEC and indicative of good capacitive behaviour (see Figure 9a and 9b) [64]. The capacities and capacitances of such a Li-HEC is shown in Figure 10.

After three formation cycles at 1 mV s^{-1}, the Li-HEC using the composite as active material showed good capacity retention (65 %) over 3000 cycles at 5 mA cm^{-2}.

To better compare these results to similar systems in the literature, power and energy densities were calculated using Equations (10), (11) and (12) to further investigate the performance:

$$P = \Delta V\ (I/m) \quad (10)$$

$$E = P\ (t/3600) \quad (11)$$

$$\Delta V = (E_{max} + E_{min})/2 \quad (12)$$

Where E_{max} and E_{min} were the potentials at the beginning and the end of the discharge, therefore, ΔV gave the average potential (V), I was the current (A), m was the mass of the active materials in both anode and cathode (kg) and t was the discharge time (s).

The TiO_2/MoO_2//AC Li-HEC showed high energy density of 44 Wh kg^{-1} at a moderate power density of 600 W kg^{-1} and even at a power density of 2700 W kg^{-1} it demonstrated an energy density of 15 Wh kg^{-1}. To demonstrate the performance of the devices, a Ragone graph was plotted in Figure 11, showing the data herein, alongside similar systems in the literature employing different anode materials, including TiO_2-reduced graphene oxide [63,68], anatase TiO_2 [63], $Li_4Ti_5O_{12}$ [68,69], TiO_2-B [70], TiO_2(B) [71], $LiCrTiO_4$ [72], Ti_9O_{17} [73], and TiO_2 microspheres wrapped with graphene nanosheets (against a graphene nanosheet positive electrode) [74].

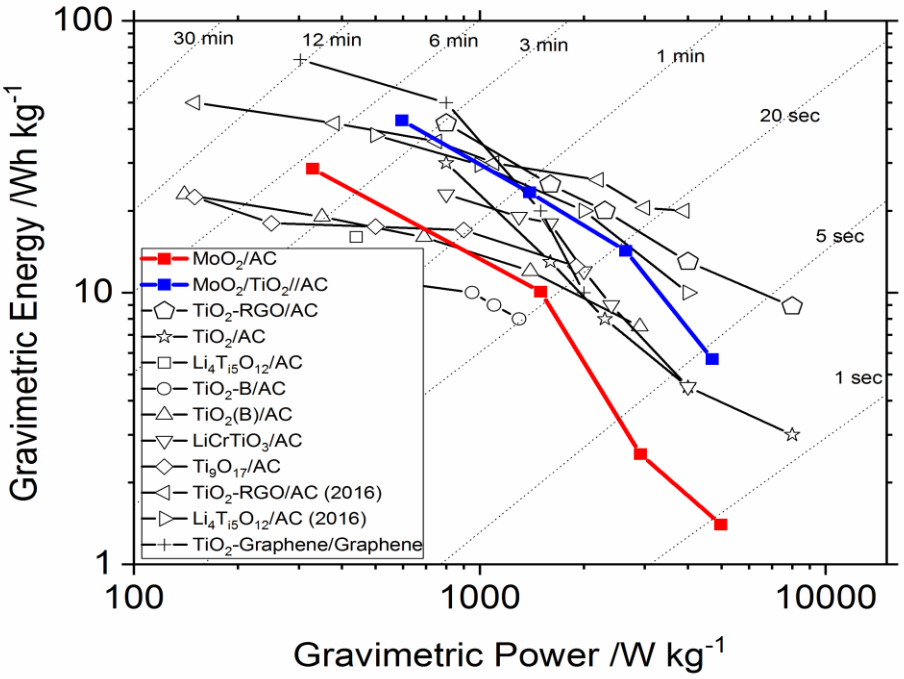

Figure 11: Ragone plot of the results herein compared to devices using anodes such as TiO_2-Reduced Graphene oxide and anatase TiO_2 [63], $Li_4Ti_5O_{12}$ [69], TiO_2-B [70], TiO_2(B) [71], $LiCrTiO_4$ [72], Ti_9O_{17} [73], TiO_2-Reduced Graphene oxide (2016) and $Li_4Ti_5O_{12}$ (2016) [68], TiO_2 microspheres wrapped with graphene nanosheets versus a graphene nanosheet positive electrode [74].

4. CONCLUSIONS

Nano-sized MoO_2 and a TiO_2/MoO_2 nanocomposite were separately synthesised using a one-step continuous hydrothermal flow synthesis method. Adding 20 mol% titanium salt in the precursor feed containing the Mo salt significantly improved reaction yield and reduced the size of MoO_2 particles, which resulted in a fivefold increase in surface area.

The chemical resistance and structural stability of TiO_2 in the composite material significantly improved cycle life in Li-ion half-cells. The reduced average particle size increased lithium-ion diffusion and facilitated larger pseudocapacitive contributions to charge storage, which led to better high-rate performance compared to pure MoO_2. The improved cycling stability of the composite was believed to be a result of TiO_2 acting as a buffer and anchor for Mo and MoO_2 during excessive volume change.

The composite material showed significantly better high-rate performance with a specific discharge capacity of 150 mAh g^{-1} at 5 A g^{-1} and better cycle life than the pure MoO_2 anodes. The composite also showed higher specific capacities than pure TiO_2 electrodes cycled in the same potential window. A Li-HEC using TiO_2/MoO_2 as active material in its anode and an activated carbon cathode showed high energy densities of 44 Wh kg^{-1} and 15 Wh kg^{-1} at power densities of 600 W kg^{-1} and 2700 W kg^{-1}, respectively.

Acknowledgements

The EPSRC are thanked for funding the Centre for Doctoral Training in Molecular Modelling & Materials Science (UCL, UK) and JAIST (Kanazawa, Japan) are thanked for supporting a studentship for DB. JAD, DJLB and PRS thank EPSRC for support of the ELEVATE (ELEctrochemical Vehicle Advanced TEchnology) low carbon vehicles project (EPSRC Ref. EP/M009394/1).

References

1. Arunabha Ghosg and Young Lee, *ChemsucChem*, 5 (2012) 797.
2. Zhang W J, *J. Power Sources*, 196 (2011) 13.
3. Armand M and Tarascon J-M, *Nature*, 451 (2008) 652.
4. Tarascon J M and Armand M, *Nature*, 414 (2001) 359.
5. Lin C, Ding B, Xin Y, Cheng F, Lai M O, Lu L and Zhou H, *J. Power Sources*, 248 (2014) 1034.
6. Palacín M R, *Chem. Soc. Rev.*, 38 (2009) 2565.
7. Winter M and Brodd R J, *Chem. Rev.*, 104 (2004) 4245.
8. Ibrahim H, Ilinca A and Perron J, *Renew. Sustain. Energy Rev.*, 12 (2008) 1221.
9. Chen Z, Augustyn V, Jia X, Xiao Q, Dunn B and Lu Y, *ACS Nano*, 6 (2012) 4319.
10. Zuo W, Li R, Zhou C, Li Y, Xia J and Liu J, *Adv. Sci.*, (2017) 1600539.
11. Aravindan V, Gnanaraj J, Lee Y-S and Madhavi S, *Chem. Rev.*, 114 (2014) 11619.
12. Kim H-S, Cook J B, Tolbert S H and Dunn B, *J. Electrochem. Soc.*, 162 (2015) A5083.
13. Johnson I D, Blagovidova E, Dingwall P A, Brett D J L, Shearing P R and Darr J A, *J. Power Sources*, 326 (2016) 476.
14. Wang J, Polleux J, Lim J and Dunn B, *J. Phys. Chem. C*, 111 (2007) 14925.
15. Lübke M, Shin J, Marchand P, Shearing P, Brett D, Liu Z and Darr J A, *J. Mater. Chem. A*, 3 (2015) 22908.
16. Bauer D, Roberts A J, Matsumi N and Darr J A, *Nanotechnology*, 28 (2017) 195403.
17. Dylla A G, Henkelman G and Stevenson K J, *Acc. Chem. Res.*, 46 (2013) 1104.
18. Liu H, Bi Z, Sun X-G, Unocic R R, Paranthaman M P, Dai S and Brown G M, *Adv. Mater.*, 23 (2011) 3450.
19. Kumar Sen U, Shaligram A and Mitra S, *ACS Appl. Mater. Interfaces*, 6 (2014) 14311.

20. Shi Y, Guo B, Corr S A, Shi Q, Hu Y S, Heier K R, Chen L, Seshadri R and Stucky G D, *Nano Lett.*, 9 (2009) 4215.
21. Guo B, Fang X, Li B, Shi Y, Ouyang C, Hu Y S, Wang Z, Stucky G D and Chen L, *Chem. Mater.*, 24 (2012) 457.
22. Sun Y, Hu X, Luo W and Huang Y, *J. Mater. Chem.*, 22 (2012) 425.
23. Xu Y, Yi R, Yuan B, Wu X, Dunwell M, Lin Q, Fei L, Deng S, Andersen P, Wang D and Luo H, *J. Phys. Chem. Lett.*, 3 (2012) 309.
24. Xia F, Hu X, Sun Y, Luo W and Huang Y, *Nanoscale*, 4 (2012) 4707.
25. Zhu K, Wang Q, Kim J H, Pesaran A A and Frank A J, *J. Phys. Chem. C*, 116 (2012) 11895.
26. Auborn J J and Barberio Y L, *J. Electrochem. Soc.*, 134 (1987) 638.
27. Ku J H, Jung Y S, Lee K T, Kim C H and Oh S M, *J. Electrochem. Soc.*, 156 (2009) A688.
28. Paul B, Kishor J and Suri A K, (2013) 31.
29. Li S, *Int. J. Electrochem. Sci.*, 13 (2018) 23.
30. Kim S E, Kim K W, Lee S W, Kim S O, Kim J S and Lee J K, *Curr. Appl. Phys.*, 13 (2013) 1923.
31. Zhu X, Yang C, Xiao F, Wang J and Su X, *New J. Chem.*, 39 (2015) 683.
32. Lee B G, Nam S C and Choi J, *Curr. Appl. Phys.*, 12 (2012) 1580.
33. Wang D, Choi D, Yang Z, Viswanathan V V, Nie Z, Wang C, Song Y, Zhang J and Liu J, *Chem. Mater.*, (2008) 3435.
34. Cheng Q, *Int. J. Electrochem. Sci.*, c (2018) 265.
35. Liang Y, Yi Z, Yang S, Zhou L, Sun J and Zhou Y, *Solid State Ion.*, 177 (2006) 501.
36. Choi H, Heo J H, Ha S, Kwon B W, Yoon S P, Han J, Kim W S, Im S H and Kim J, *Chem. Eng. J.*, 310 (2017) 179.
37. Marin-Flores O, Turba T, Ellefson C, Wang K, Breit J, Ahn J, Norton M G and Ha S, *Appl. Catal. B Environ.*, 98 (2010) 186.
38. Liu X, Ji W, Liang J, Peng L and Hou W, *Phys. Chem. Chem. Phys.*, 16 (2014) 20570.
39. Darr J A and Poliakoff M, *Chem. Rev.*, 99 (1999) 495.
40. Zhang Z, Goodall J B M, Brown S, Karlsson L, Clark R J H, Hutchison J L, Rehman I U and Darr J a, *Dalton Trans.*, 39 (2010) 711.
41. Adschiri T, Lee Y-W, Goto M and Takami S, *Green Chem.*, 13 (2011) 1380.
42. Darr J A, Zhang J, Makwana N M and Weng X, *Chem. Rev.*, 117 (2017) 11125.
43. Chen M, Ma C Y, Mahmud T, Darr J A and Wang X Z, *J. Supercrit. Fluids*, 59 (2011) 131.
44. Gruar R I, Tighe C J and Darr J A, *Ind. Eng. Chem. Res.*, 52 (2013) 5270.
45. Darr J A, Tighe C J and Gruar R I, (United States: US2013/0136687 A1.)
46. Katrib A, Sobczak J W, Krawczyk M, Zommer L, Benadda A, Jablonski A and Maire G, *Surf. Interface Anal.*, 34 (2002) 225.
47. Baltrusaitis J, Mendoza-Sanchez B, Fernandez V, Veenstra R, Dukstiene N, Roberts A and Fairley N, *Appl. Surf. Sci.*, 326 (2015) 151.
48. Deng Z, Hu Y, Ren D, Lin S, Jiang H and Li C, *Chem. Commun. (Camb).*, 51 (2015) 13838.
49. Zhang Z, Brown S, Goodall J B M, Weng X, Thompson K, Gong K, Kellici S, Clark R J H, Evans J R G and Darr J A, *J. Alloys Compd.*, 476 (2009) 451.
50. Zeng L, Zheng C, Deng C, Ding X and Wei M, *ACS Appl. Mater. Interfaces*, 5 (2013) 2182.
51. Van De Krol R, Goossens A and Schoonman J, *J. Phys. Chem. B*, 103 (1999) 7151.
52. Das S K, Gnanavel M, Patel M U M, Shivakumara C and Bhattacharyya A J, *J. Electrochem. Soc.*, 158 (2011) A1290.
53. Randles J E B, *Trans. Faraday Soc.*, 44 (1948) 327.
54. Augustyn V, Simon P and Dunn B, *Energy Environ. Sci.*, 7 (2014) 1597.
55. Augustyn V, Come J, Lowe M a, Kim J W, Taberna P-L, Tolbert S H, Abruña H D, Simon P and Dunn B, *Nat. Mater.*, 12 (2013) 518.
56. Bresser D, Paillard E, Copley M, Bishop P, Winter M and Passerini S, *J. Power Sources*, 219

(2012) 217.
57. Lübke M, Johnson I, Makwana N M, Brett D, Shearing P, Liu Z and Darr J A, *J. Power Sources*, 294 (2015) 94.
58. Yang Y, Bai Y, Zhao S, Chang Q and Zhang W, *J. Alloys Compd.*, 579 (2013) 7.
59. Zhu X, Liang X, Fan X and Su X, *RSC Adv.*, 7 (2017) 38119.
60. Braun P V., Cho J, Pikul J H, King W P and Zhang H, *Curr. Opin. Solid State Mater. Sci.*, 16 (2012) 186.
61. Li J, Dozier A K, Li Y, Yang F and Cheng Y-T, *J. Electrochem. Soc.*, 158 (2011) A689.
62. Luo Y, Luo J, Jiang J, Zhou W, Yang H, Qi X, Zhang H, Fan H J, Yu D Y W, Li C M and Yu T, *Energy Environ. Sci.*, 5 (2012) 6559.
63. Kim H, Cho M-Y, Kim M-H, Park K-Y, Gwon H, Lee Y, Roh K C and Kang K, *Adv. Energy Mater.*, 3 (2013) 1500.
64. Vanchiappan A, *J. Mater. Chem. A*, (2013) 707.
65. Yin J, Qi L and Wang H, *ACS Appl. Mater. Interfaces*, 4 (2012) 2762.
66. Liu X, Zhang N, Ni J and Gao L, *J. Solid State Electrochem.*, 17 (2013) 1939.
67. Arun N, Jain A, Aravindan V, Jayaraman S, Chui Ling W, Srinivasan M P and Madhavi S, *Nano Energy*, 12 (2015) 69.
68. Kim H K, Mhamane D, Kim M S, Roh H K, Aravindan V, Madhavi S, Roh K C and Kim K B, *J. Power Sources*, 327 (2016) 171.
69. Ni J, Yang L, Wang H and Gao L, *J. Solid State Electrochem.*, 16 (2012) 2791.
70. Wang Q, Wen Z and Li J, *Adv. Funct. Mater.*, 16 (2006) 2141.
71. Aravindan V, Shubha N, Ling W C and Madhavi S, *J. Mater. Chem. A*, 1 (2013) 6145.
72. Aravindan V, Chuiling W and Madhavi S, *J. Mater. Chem.*, 22 (2012) 16026.
73. Han W-Q and Wang X-L, *Appl. Phys. Lett.*, 97 (2010) 2431041.
74. Wang F, Wang C, Zhao Y, Liu Z, Chang Z, Fu L, Zhu Y, Wu Y and Zhao D, *Small*, (2016) 1.